Title

A Pore-Scale Investigation of Mineral Precipitation Driven Diffusivity Change at the Column-Scale

Journal

Water Resources Research, 57(5)

ISSN

0043-1397

Authors

Deng, H
Tournassat, C
Molins, S
et al.

Publication Date

2021-05-01

DOI

10.1029/2020wr028483

Peer reviewed

AGU ADVANCING EARTH AND SPACE SCIENCE

Water Resources Research

RESEARCH ARTICLE
10.1029/2020WR028483

A Pore-Scale Investigation of Mineral Precipitation Driven Diffusivity Change at the Column-Scale

H. Deng[1], C. Tournassat[1,2,3], S. Molins[1], F. Claret[2], and C. I. Steefel[1]

[1]Energy Geosciences Division, Lawrence Berkeley National Laboratory, Berkeley, CA, USA, [2]BRGM, Orléans, France, [3]Institut des Sciences de la Terre d'Orléans, Université d'Orléans—CNRS/INSU—BRGM, Orléans, France

Key Points:

- Pore-scale reactive transport modeling of diffusion controlled mineral precipitation
- Examined the evolution of pore structures and averaged bulk properties
- Developed modified porosity-diffusivity relationship that accounts for pore-scale mineral precipitation dynamics

Supporting Information:

Supporting Information may be found in the online version of this article.

Correspondence to:

H. Deng,
hangdeng@lbl.gov

Citation:

Deng, H., Tournassat, C., Molins, S., Claret, F., & Steefel, C. I. (2021). A pore-scale investigation of mineral precipitation driven diffusivity change at the column-scale. *Water Resources Research*, *57*, e2020WR028483. https://doi.org/10.1029/2020WR028483

Received 27 JUL 2020
Accepted 18 APR 2021

Abstract

Mineral precipitation affects the pore structure and thus transport properties of porous media. In this study, we investigated the pore-scale dynamics of precipitation in diffusion controlled systems and the resulting impacts on the effective diffusivity, using a micro-continuum reactive transport model. Forty two-dimensional pore structures representing both idealized and realistic geometries were simulated with consideration of different precipitation scenarios and rates. A homogeneous nucleation scenario reproduced patterns observed in previous experimental study showing mixing-induced precipitation, and a surface growth scenario captured the pattern for mineral precipitation on a substrate with the same or similar mineral structures. In all cases, local precipitation resulted in the reduction in the average porosity of the domain (Φ) until the cessation of diffusive transport and the termination of precipitation. The minimum porosity reached was referred to as the critical porosity (Φ_c). The effective diffusivity (D_{eff}) decreased with Φ and dropped sharply to effectively zero, that is, the critical effective diffusivity (D_{effc}), as Φ_c was reached. These pore-scale dynamics can be captured by a revised $\Phi - D_{\text{eff}}$ relationship that explicitly considers the critical porosity and the corresponding effective diffusivity, and the pre-exponential coefficient and the exponent of the relationship varied with initial pore structure and the precipitation kinetics. Overall, the homogeneous nucleation scenario results in systematically larger Φ_c and coefficients that give rise to a sharper decrease in diffusivity as Φ_c is approached, compared to the surface growth scenario. The revised relationship was also implemented at continuum scale and used to examine column scale diffusivity change and reactions.

Plain Language Summary

Mineral precipitation alters the internal structures of geo-materials, and thus affects how fluid and solutes migrate in these porous media. Typically, this alteration has been modeled by assuming that the changes in transport properties are proportional to the amount of mineral precipitation, following a simple power law function. However, previous experimental studies have pointed out that in addition to the amount of mineral precipitation, how the structures of porous media are altered by the mineral precipitates can be important as well. In our study, we used numerical modeling that resolves the geometry of porous media explicitly to investigate how the structures evolve as a result of mineral precipitation. In these simulations, we consider initial geometry of different complexity and a range of precipitation rates that have been reported in previous studies. All the simulations showed that a small amount of precipitation can result in plugging of the porous media, by clogging a small portion of the transport pathways. Based on the simulation results, we demonstrated that the simple power law function can be modified to account for these structural changes. We have also implemented this modified power law relationship to simulate a column experiment published previously and showed good agreements.

1. Introduction

Mineral dissolution and precipitation can change the structures of fractured porous media, and thus control their mechanical and hydrodynamic properties. Mineral precipitation is widely observed and occurs when the fluid is over-saturated with respect to one or multiple mineral phases. Some conditions that can be encountered in natural and engineered systems and lead to mineral precipitation include (i) solubility change, for example, due to the presence of temperature gradients (Griffiths et al., 2016; Steefel & Lasaga, 1994), (ii) mixing of fluids (Emmanuel & Berkowitz, 2005; Tartakovsky et al., 2008), and (iii) mineral dissolution that increases the concentration of key chemical species (Garcia-Rios et al., 2015; Li et al., 2017; Seigneur et al., 2019; Steefel & Lichtner, 1994; Xie et al., 2015). Understanding and predicting the evolution of Earth's

systems resulting from mineral precipitation are important. For instance, mineralization of CO_2 injected into the underground as part of geologic carbon storage is an important permanent trapping mechanism (Matter et al., 2016), and mineral precipitation can affect the efficiency of hydraulic fracturing and the performance of other subsurface energy applications (Vankeuren et al., 2017). In addition, salt precipitation alters the hydraulic properties of soils (Nachshon et al., 2011) and the porosity in coastal environments, especially in the saltwater-freshwater mixing zones (Singurindy et al., 2004). Mineral precipitation is one mechanism used to scavenge contaminants in aquifers (Wright et al., 2011), a by-product of remediation technologies such as *in situ* chemical oxidation (Chen and Park, 2017), and can reduce the efficiency of membranes used for water desalination (Rahardianto et al., 2008). Therefore, evaluating and predicting mineral precipitation and its impacts on porous media are needed for improving management practices of soils and groundwater resources.

In continuum scale modeling (Lichtner, 1996; Steefel & Lichtner, 1994; 1998; Steefel et al., 2005; Steefel, Appelo, et al., 2015), the changes in flow and transport properties resulting from mineral precipitation, and mineral reactions in general, are typically described by power law functions of porosity (ϕ). Commonly used functional relations include the Kozeny-Carman relationship between porosity and permeability and Archie's law that relates effective diffusivity to porosity. These relationships are easy to implement and allow some considerations of system specificity such as textural heterogeneity through the empirical coefficients (Cai et al., 2017; Luquot & Gouze, 2009; Menke et al., 2017; Peng et al., 2012; Smith et al., 2013; Steinwinder & Beckingham, 2019).

However, adjusting the parameters alone in some cases fails to produce flow and transport properties that are directly measured or inferred from observations. In flow-through experiments in carbonate rocks with induced precipitation (Luquot & Gouze, 2009), it is observed that porosity-permeability relationship shifted away from a power law relationship as precipitation progresses. Navarre-Sitchler et al. (2009) performed diffusion experiments on weathered basalt samples and the corresponding parent materials and showed that the effective diffusivity (D_{eff}) evaluated using micro-x-ray fluorescence spectroscopy cannot be fitted with a simple form of Archie's law given by $D_{\text{eff}} = D_m a \phi^m$, where D_m is the molecular diffusion coefficient and a and m are the empirical coefficients. In Chagneau et al. (2015), a set of column experiments were carried out to assess the changes in the effective diffusivity of the system as a result of mineral precipitation. In the study of Chagneau et al. (2015), a one-dimensional continuum reactive transport model using Archie's law either over-estimated the amount of precipitation or over-estimated the tracer transport.

These studies highlighted the need of further development of constitutive relations or other means to account for pore-scale dynamics that are not captured by bulk averaged parameters used in continuum scale modeling. For this purpose, pore-scale experiments and modeling have been used to investigate microscopic scale dynamics that arise from geometric and mineralogical heterogeneity and that can propagate to larger scale processes (Cil et al., 2017; Deng et al., 2018; Chen et al., 2014; Molins et al., 2020; Zhang, Kang, et al., 2010). For system evolution driven by mineral precipitation, the complexity of pore-scale dynamics is compounded by the processes of nucleation and crystal growth. It was shown that the morphology and texture of the precipitates depend on the substrates (Noiriel et al., 2016), supersaturation (Kim et al., 2020; Rajyaguru et al., 2019; Zhang, Dehoff, et al., 2010), and local hydrodynamics (Poonoosamy et al., 2019). Parallel pore-scale modeling studies were used to simulate precipitation patterns (Yoon et al., 2012), and their dependence on fluid saturation (Prasianakis et al., 2017). Pore-scale models were also used to examine system evolution and their dependence on different nucleation mechanisms, for example, epitaxial crystal growth versus crystal growth along the direction of maximum concentration gradient or probabilistic nucleation versus deterministic nucleation (Fazeli et al., 2020; Chen et al., 2014).

These studies with well controlled and characterized experiments and high-fidelity modeling have provided valuable data and important mechanistic understanding of precipitation-driven pore-scale dynamics. While a few studies have examined permeability evolution following precipitation and its relationship with respect to porosity change (Fazeli et al., 2020; Noiriel et al., 2016), how pore-scale dynamics translate into continuum scale transport properties remains an open question. In our study, we aim to use carefully designed pore-scale reactive transport simulations to address this gap. The complexity and uncertainties of precipitation kinetics were considered by including different precipitation scenarios and rates. In the following sections, we first present the model and simulation approach and then follow this with pore-scale

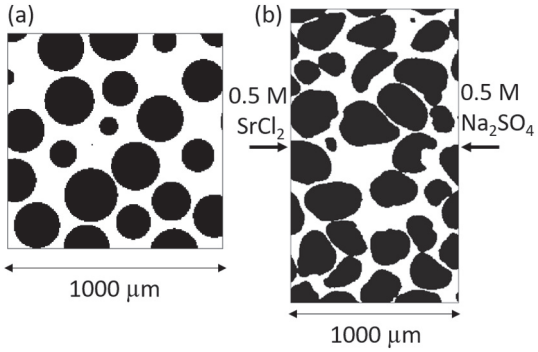

Figure 1. Illustration of the 2D domains of (a) the Finney pack geometry and (b) the quartz sand pack geometry, and of the fluid chemistry boundary conditions used in the simulations.

simulation results and discussions of the revised mathematical relation that integrates the pore-scale dynamics into column/continuum scale simulations.

2. Methods

The approach taken in this work is the simulation of diffusion-reaction processes in 2D domains derived from openly available digital rock data. The simulations were performed systematically under different model assumptions and over a range of parameters. The simulations used the solution chemistry and major physical bulk properties of the experimental work of Chagneau et al. (2015), in which celestite precipitation was induced in the quartz sand packed column by the mixing of a Sr-rich fluid and a sulfate-rich fluid introduced via diffusion from the two ends, respectively. This allowed us to leverage the experimental data for comparison and discussion. The precipitation reaction writes as follows. All aqueous reactions and the corresponding equilibrium constants are summarized in the supporting information.

$$Sr^{2+} + SO_4^{2-} \rightarrow SrSO_4(s). \tag{1}$$

2.1. Pore Geometry

Two pore geometries were considered, using data archived at the digital rock portal (https://www.digitalrocksportal.org/). One data set represents an idealized geometry from a random packing of hard spheres with uniform radii (Finney, 2016). A three-dimensional (3D) volume image was generated using the reported coordinates of the sphere centers, using a radius of 150 μm and a voxel size of 5 μm. The voxel size was representative of the resolution of micro-tomography images, and the diameter was comparable to the grain size used in the experiments of Chagneau et al. (2015). The other data set included grayscale synchrotron x-ray computed tomography images of a column that was packed with quartz sands of grain sizes of 420–600 μm (Molnar, 2016). The images had a resolution of 9.87 μm and were rescaled to a resolution of 5 μm such that the grain sizes were comparable with the Finney pack geometries. For the simulations, the CT images from Molnar (2016) were segmented in MATLAB using Otsu's method (Otsu, 1979) to generate a binary volume image. The average porosity of the middle section of the Finney pack was 48%, whereas the average porosity of the quartz pack was 33%. These values are on the higher and lower end of the values reported for the experimental columns (42% ± 9%), respectively.

For our simulations, twenty two-dimensional (2D) domains were randomly selected from each 3D volume, as illustrated in Figure 1. The domain size was 1 by 1 mm (200 by 200 grid cells) for the Finney pack geometries (numbered as FGeo1-20) and was 1 by 1.75 mm (200 by 350 grid cells) for the quartz pack geometries (numbered as QGeo1-20). The width was larger for the quartz pack geometries to ensure initial connectedness of the domain.

2.2. Reactive Transport Model for Precipitation Simulations

In our study, the code CrunchTope (Steefel, Appelo, et al., 2015) was used for all the reactive transport simulations. For pore-scale simulations, modifications were made to implement the micro-continuum approach: the pore geometry was explicitly represented, whereas porosity was used to keep track of partial volume in individual grid cells due to precipitation. As the system considered was diffusion controlled, the main governing equation written with respect to the total concentration of a chemical component Ψ_i is given as follows:

$$\frac{\partial \phi \Psi_i}{\partial t} = \nabla \cdot \left(\phi D \nabla \Psi_i\right) - \vartheta_i R_i, \tag{2}$$

where the local porosity (ϕ) is 1.0 in the pore space, 0.0 inside the mineral grains and is a fractional value as precipitation progresses and occupies part of the grid cell. D is the diffusion coefficient, which is equal to the molecular diffusion coefficient in the pore space, and is $D_m\phi$ in grid cells occupied by the precipitates to account for the tortuosity caused by the presence of the solid phase. Two additional non-linear tortuosity models ($D = D_m\phi^{n_0}$, $n_0 = 2\ or\ 3$) were also tested for a subset of the simulation conditions to examine the impacts of this assumption. For simplicity, we assumed that the molecular diffusion for all aqueous species is the same, with $D_m = 2.24 \times 10^{-9}$ m^2/s following that of the tracer in Chagneau et al. (2015). The total concentration is the sum of the concentration of the primary species and those of other species that can be expressed in terms of the primary species based on mass action laws. The concentrations of all primary species were calculated by solving the mass balance equation (Equation 2). Spatial discretization for numerically solving Equation 2 followed the image resolution.

The reaction term (last term on the right hand side) accounts for the concentration change caused by mineral reactions, with ϑ_i being the stoichiometric coefficient and one for celestite. Two precipitation conceptualizations were considered to bracket different reaction mechanisms. In one scenario, homogeneous nucleation was enabled in the pore space and provided the initial surface area for subsequent crystal growth. This is referred to as the homogeneous nucleation (HN) scenario. In the other scenario, referred to as the surface growth (SG) scenario, homogeneous nucleation in the pore space was not enabled. This is also equivalent of assuming that heterogeneous nucleation is fast and crystal growth picks up immediately.

$$R_i = \begin{cases} R_{i,nuc} + R_{i,tst}, & for\ HN \\ R_{i,tst}, & for\ SG \end{cases}. \tag{3}$$

Crystal growth rate was calculated from the transition state theory rate law ($R_{i,\mathrm{tst}}$ [mol / m^{3}s]) and is positive for the precipitation reaction.

$$R_{i,\mathrm{tst}} = \mathrm{Ak}_{rxn} \prod a_j^{n_j} \exp\left(-\frac{E_a}{\mathrm{RT}}\right)\left(1 - \left(\frac{\mathrm{IAP}}{K_{\mathrm{sp}}}\right)^{m_1}\right)^{m_2}. \tag{4}$$

where $A\left(\mathrm{m}^2 / \mathrm{m}^3\right)$ is the bulk surface area of the mineral, $k_{rxn}\left(\mathrm{mol} / \mathrm{m}^2\mathrm{s}\right)$ is the kinetic factor, a_j is the activity of any catalytic and inhibitory species, and n_j is the corresponding reaction order. The Arrhenius term accounts for the temperature ($T[K]$) effect, where $E_a\left(\mathrm{J} / \mathrm{mol}\right)$ is the activation energy, and $R\left(\mathrm{J/mol\,K}\right)$ is the ideal gas constant. The thermodynamic driving force is measured by the saturation index, which is the ratio of ionic activity product (IAP) to solubility (K_{sp}), and m_1 and m_2 are constants dependent on the reaction mechanisms.

Homogeneous nucleation rate ($R_{i,\mathrm{nuc}}$ [mol / m^{3}s]) was described by the classical nucleation theory and was implemented in CrunchTope as follows (Li et al., 2017):

$$R_{i,nuc} = A_0 J_0 exp - \left(\frac{16\pi v^2 \alpha^3}{3k_B^3 T^3 \left(\ln\left(\frac{IAP}{K_{sp}}\right)\right)^2} \right) \tag{5}$$

where A_0 is unity (m^2 / m^3) and J_0 is the kinetic factor with a value of 1.0×10^{-8} mol/m^{2}s for celestite, which is within the range inferred from the experimental study of Poonoosamy et al. (2019). v is the molecular volume (8.21×10^{-29} m^3 for celestite), α is the effective interfacial tension (0.092 J/m^2 for celestite, Nielsen & Söhnel, 1971), and k_B is the Boltzmann constant. It is assumed that the nuclei formed via homogeneous nucleation stay in the same grid cell, where the crystal growth continues.

For the homogeneous nucleation scenario, at a given time (t), the surface area used in Equation 4 was calculated as

Table 1
The Kinetic Data and Surface Area Setup for Different Precipitation Scenarios Simulated in This Study

Scenario	Nucleation	Crystal growth kinetic data	Surface area	Reference
Homogeneous nucleation	$\alpha = 0.092\,\mathrm{J/m^2}$ *	$k_{rxn} = k_{Marty}$	Specific surface area 0.44 m^2/g	ssa0.44
	$J_0 = 1.0\times10^{-8}$ mol / m^2s**	$m_1 = 0.5, m_2 = 2$		
		$\log k_{Marty} = -7.23$ ***		
	$\alpha = 0.092\,\mathrm{J/m^2}$	$k_{rxn} = k_{usgs} a_{H^+}^{0.109}$	Specific surface area 0.44 m^2/g	ssa0.44_usgs
	$J_0 = 1.0\times10^{-8}$ mol / m^2s	$m_1 = m_2 = 1$		
		$\log k_{usgs} = -5.66$ ****		
	$\alpha = 0.092\,\mathrm{J/m^2}$	$k_{rxn} = k_{Marty}$	Specific surface area 44 m^2/g	ssa44
	$J_0 = 1.0\times10^{-8}$ mol / m^2s	$m_1 = 0.5, m_2 = 2$		
		$\log k_{Marty} = -7.23$		
Surface growth	N/A	$k_{rxn} = k_{Marty}$	Porosity gradient area	pga
		$m_1 = 2, m_2 = 0.5$		
		$\log k_{Marty} = -7.23$		
	N/A	$k_{rxn} = k_{usgs} a_{H^+}^{0.109}$	Porosity gradient area	pga_usgs
		$m_1 = m_2 = 1$		
		$\log k_{usgs} = -5.66$		

The data are from *Nielsen & Söhnel (1971), **Poonoosamy et al. (2019), ***Marty et al. (2015), and **** Palandri (2004).

$$A = \mathrm{MW}\cdot \mathrm{ssa}\cdot \int_0^t R_i, \tag{6}$$

where $\mathrm{MW}\left(\mathrm{g/mol}\right)$ is the molecular weight and ssa is the specific surface area (m^2/g).

For the surface growth scenario, the surface area used in Equation 4 was the geometric surface area of the solid phase and was calculated based on the pore geometry as the gradient of the local porosity using the micro-continuum formulation derived from the volume averaging theorem (Soulaine et al., 2017 and references therein):

$$A = \left|\nabla\phi\right|. \tag{7}$$

In order to account for uncertainties introduced by the kinetic data, two sets of kinetic coefficients and two specific surface areas were examined in the simulations. One kinetic formulation followed Palandri (2004) and included a non-linear dependence on pH. The other kinetic formulation used was from Marty et al. (2015) and was independent of any other species. The specific surface area of celestite varies substantially, as reported in Chagneau et al. (2015). Accordingly, two values, 0.44 and 44 m^2/g, were chosen as the bounding cases. Overall, higher specific surface area and the kinetic coefficient from Marty et al. (2015) would result in higher reaction rate. The parameters and kinetic scenarios are summarized in Table 1.

Mineral precipitation was used to update local porosity:

$$\phi^{t+dt} = \phi^t - R_i V_m dt, \tag{8}$$

where V_m is the molar volume of celestite and dt is the time step.

The precipitation simulations used boundary conditions similar to the experiment. The two ends of the computational domain were assigned a Dirichlet boundary condition, in contact with a solution of 0.5 M $SrCl_2$ and a Na_2SO_4 solution of 0.5 M, respectively (Figure 1). The other two sides were assigned no flux boundary conditions.

2.3. Numerical Tracer Experiments

During the precipitation simulations, pore structures were recorded at multiple time points. Numerical tracer experiments were performed to evaluate the corresponding effective diffusivity, similar in concept and execution to those considered by Navarre-Sitchler et al. (2009) and Steefel, Beckingham, & Landrot (2015). The governing equation of the numerical tracer experiments was similar to the precipitation simulations but without the reaction term.

$$\frac{\partial \phi C_{\text{tracer}}}{\partial t} = \nabla \cdot \left(\phi D \nabla C_{\text{tracer}}\right). \tag{9}$$

In the tracer simulations, the Dirichlet boundary on the left was considered as the inlet and was exposed to a solution with a non-reactive tracer of 1 M. The pairing boundary, that is, the outlet, had a zero-gradient boundary condition and is where the tracer break-through curve ($C_{\text{tracer}}\left(t\right)|_{x=L}$) was monitored. Other boundary conditions, spatial discretization, and diffusion coefficients were set up in the same way as the precipitation simulations.

The effective diffusivity (D_{eff}) is the bulk transport property of the entire computational domain and is evaluated by fitting the tracer break-through curve from the numerical tracer experiments using the one-dimensional (1D) diffusion equation.

$$\frac{\partial C_{\text{tracer}}}{\partial t} = D_{\text{eff}} \frac{\partial^2 C_{\text{tracer}}}{\partial x^2}. \tag{10}$$

Its relation with respect to the domain porosity (Φ), which is the average of the local porosity in all grid cells in the domain ($\Phi = \sum_x \sum_y \phi\left(x, y\right)$), was analyzed. In the following sections, porosity refers to the domain porosity unless specified otherwise.

Numerical tracer experiments were performed for all Finney pack geometries and a subset of four quartz sand pack geometries.

3. Simulation Results

3.1. Pore Geometry Evolution and Porosity Reduction

In the homogeneous nucleation scenario, a precipitation band formed in the pore space (Figure 2a–2c). This type of pattern was observed in the microfluidic experiments by Zhang, Dehoff, et al. (2010), in which calcium-carbonate precipitation was induced by the mixing of the calcium-rich and carbonate-rich fluids in the analog porous media, and the precipitation band tracked the mixing line of the two fluids. Their experimental observation was also confirmed by the companion modeling work (Yoon et al., 2012), and the initial surface area was assumed to be provided by the top and bottom surfaces of the microfluidic cell. In our study, the initial surface area was created by the homogeneous nucleation in the fluid that was locally supersaturated.

In contrast, under the surface growth scenario, the precipitates coated the mineral grains, and the precipitation pattern was thus largely influenced by the initial pore structure (Figures 2d and 2e). This precipitation pattern was consistent with the scenario when the substrate had a similar crystal structure to the precipitating mineral. Similar patterns have been observed in the experimental study of Noiriel et al. (2012) when the injected fluid over-saturated with respect to calcium carbonate interacted with the calcite spar substrate. In these cases, heterogeneous nucleation, which was not considered in our model, is fast, and the following crystal growth is the dominant process.

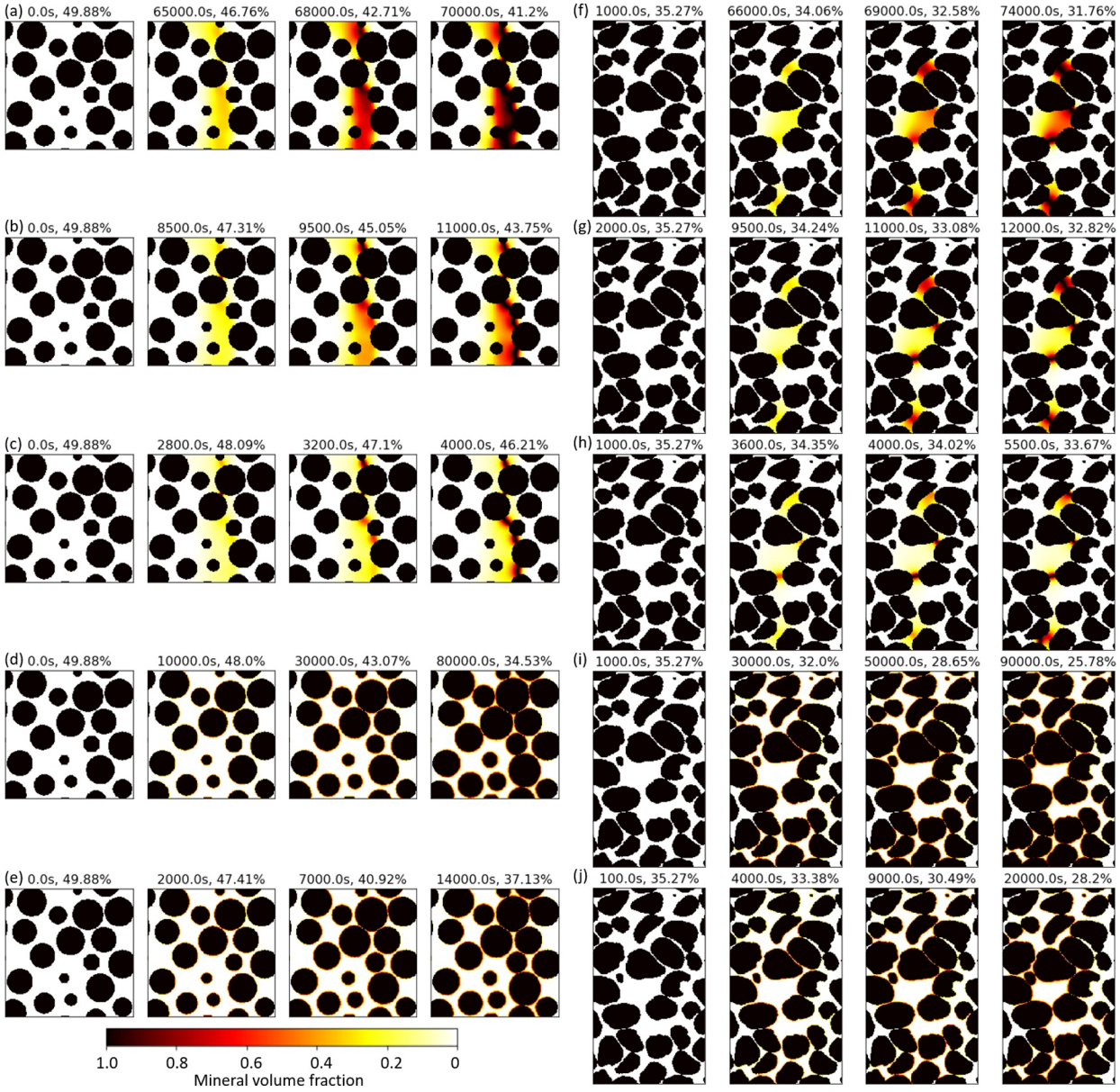

Figure 2. Snapshots of pore geometry evolution for a Finney pack geometry (a)–(e) and a quartz sand pack geometry (f)–(j) for different precipitation setups: (a) (f)—ssa0.44, (b) (g)—ssa0.44_usgs, (c) (h)—ssa44, (d) (i)—pga, (e) (j)—pga_usgs. Note that due to the difference in reaction rate and geometry, each case reached the clogging point at different time steps, and the snapshots shown are thus at different times.

Across different precipitation model setups and initial pore geometries, the domain porosity (Φ) decreased as a result of precipitation and reached a non-zero constant value afterward (Figure 3), indicating that the precipitation reaction became inhibited. As the precipitates blocked the transport pathways, mixing of the two fluids was suppressed, and thus, the precipitation reaction was no longer sustained. Here, the average porosity within the 2D computational domain at the end of the precipitation reaction is referred to as the critical porosity (Φ_c).

Under the surface growth scenario, domain porosity decreased continuously from the beginning of the simulation until the critical porosity was reached. In comparison, in the homogeneous nucleation scenario, the domain porosity remained unchanged initially as the nucleation dominated over the crystal growth pathway. The decrease in Φ became evident once enough surface area had been created by nucleation for the crystal growth to pick up. The critical porosity tended to be lower under the surface growth scenario.

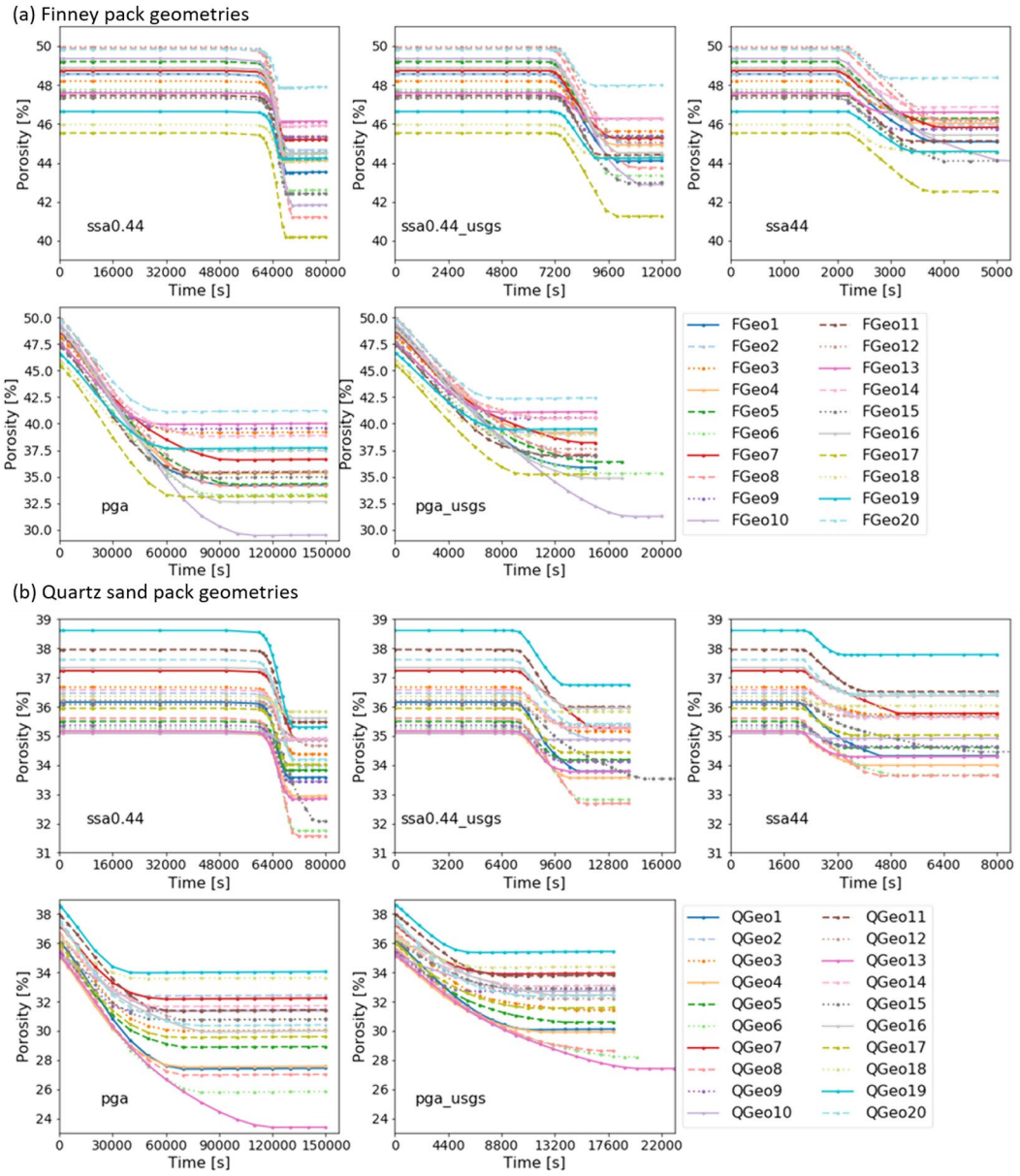

Figure 3. Domain porosity (Φ) evolution for (a) 20 Finney pack geometries (FGeo1-20) and (b) 20 quartz sand pack geometries (QGeo1-20) with different precipitation setups. Note that some cases had longer simulations as they required longer to reach the clogging time point than other cases.

For instance, for the quartz pack geometries, surface growth simulations had critical porosity as low as 24%, whereas the critical porosity of homogeneous nucleation simulations was always above 31%. This is because in the surface growth scenario, precipitation occurred on the grain surfaces outside of the pore throats were less effective in clogging the transport pathway (Figures 2d, 2e, 2i and 2j).

For the same precipitation conceptualization and geometry, a lower critical porosity was observed at a slower reaction rate. For example, in the Finney pack simulations, the critical porosity for the ssa0.44 (specific surface area = 0.44 m^2/g) case was lower than the ssa44 (specific surface area = 44 m^2/g) case by 3 percentage points. This is a result of the interplay between precipitation and diffusion, which is typically measured by the Damköhler number (Da). At the lower precipitation rate (lower Da), in grid cells that are over-saturated, less chemicals (Sr^{2+} and SO_4^{2-}) are removed from the solution by precipitation and more are transported downgradient. As a result, more grid cells become oversaturated, and by the time when the transport

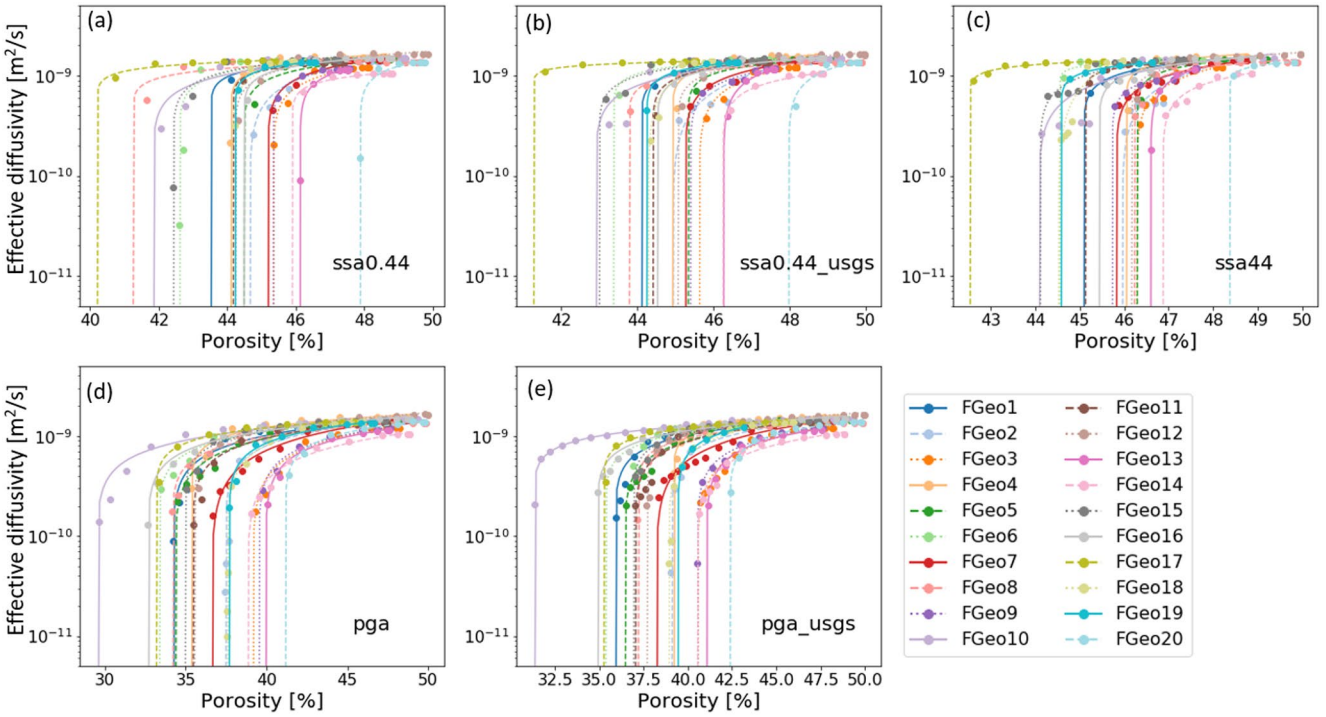

Figure 4. Effective diffusivity in relation to the porosity from the tracer simulations and the fitting line using Equation 11 for the five precipitation kinetic setups of all the Finney pack geometries (FGeo1-20). The goodness-of-fitting R^2 parameter is 0.97 on average, and larger than 0.91 for all 100 cases except for two.

paths become clogged, more precipitation would have happened. As shown in Figure 2, the precipitation band formed in the homogeneous nucleation scenario was thicker at a slower reaction rate, and the growth of the grain surfaces was observable in a wider region in the surface growth cases.

The overall reduction in the domain porosity varied between less than 1%–12% for the quartz pack geometries and between ~1% and 20% for the Finney pack geometries (Figure 3). The reduction in porosity is positively correlated with the initial porosity in the Finney pack geometries; whereas there is no clear correlation between the porosity reduction and the initial porosity for the quartz pack geometries (Figure S1). This implies that for the idealized hard sphere packing of Finney geometries, initial porosity is a good indicator of the pore structure and connectivity. In contrast, for the quartz pack geometries, there is more spatial heterogeneity in the pore structure, and porosity does not accurately reflect the connectivity of the pore structures. For instance, it was reported that permeability of sandstones from different basins does not vary monotonically with porosity and samples with comparable porosity can have different permeability and thus connectivity (Zou et al., 2012).

3.2. Effective Diffusivity Evolution

The effective diffusivity decreased with the porosity (Figure 4). The initial effective diffusivity ranged between 1.1e−9 and 1.6e−9 m^2/s in the 20 Finney pack geometries given a molecular diffusion coefficient of 2.24e−9 m^2/s for the tracer. The relatively large initial effective diffusivity was indicative of the presence of open transport pathways. As the porosity approached the clogging value, the effective diffusivity decreased significantly. At the critical porosity, the effective diffusivity became effectively zero, as evidenced by the termination of the mixing and precipitation. This was also expected in our simulations, as precipitation was allowed to proceed until local porosity (ϕ) was effectively zero (a non-zero but negligible value was used for numerical reasons). Such clogging has also been observed experimentally. In the experiments of Zhang, Dehoff, et al. (2010), dissolution of the precipitated calcium carbonate was observed at the late stage,

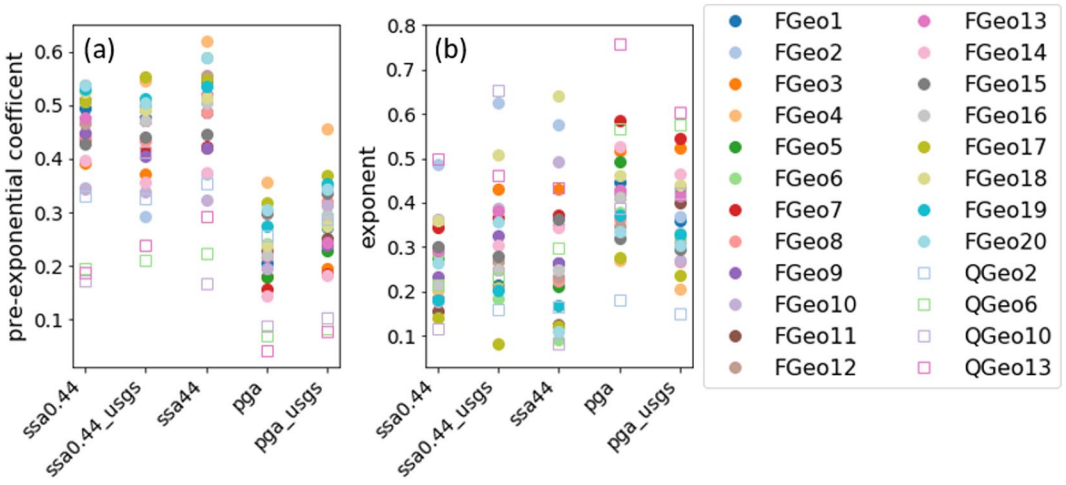

Figure 5. (a) Pre-exponential coefficient and (b) exponent of Equation 11 for all Finney pack geometries (filled circle) and the subset of quartz sand pack geometries simulated (open square) for different precipitation kinetic setups.

confirming negligible transport through the precipitates and thus the termination of mixing and further precipitation as observed in the simulations here.

These trends are consistent with what was observed in Navarre-Sitchler et al. (2009). Therefore, we accounted for the clogging effect of the precipitates on effective diffusivity by adopting the following mathematical formulation:

$$D_{\text{eff}} = D_{\text{eff}\,c} + aD_m\left(\phi - \phi_c\right)^n, \tag{11}$$

where a and n are empirical coefficients. Theoretically, the value of D_{effc} can be determined by running the numerical tracer experiment on the pore structure at the critical porosity. Here, because $D_m\phi \to 0$ when $\phi \to 0$ in the pore space that is clogged by the precipitates, $D_{\text{eff}\,c} \to 0$, as also confirmed by the numerical tracer experiments, which showed no break-through of the tracer after 10 million seconds. Therefore, a value of 1e−15 m^2/s was assumed for D_{effc} across all geometries and precipitation scenarios. This value is on the same order of magnitude as the value used for unweathered basalt rocks in Navarre-Sitchler et al. (2009) and provides a reasonable estimate for low diffusivity systems that can be encountered. Using a value of 0 or 1e−15 m^2/s for D_{effc} did not affect the evaluation of the parameters a and n. Because each simulation evolves differently and it was impossible to predict the clogging time a priori and thus set the output time steps accordingly, data points are sparse in the region where the diffusivity drops dramatically within a small porosity change and a relatively short time period.

For the Finney pack geometries (Figure 5), the pre-exponential coefficients (a) for the two surface growth cases (i.e., "pga" and "pga_usgs") were 0.24 ± 0.06 (mean ± standard deviation) and 0.29 ± 0.07, respectively, and were smaller than those for the three homogeneous nucleation cases (i.e., "ssa0.44", "ssa0.44_usgs", and "ssa44"), which were 0.46 ± 0.06, 0.45 ± 0.07, and 0.49 ± 0.08, respectively. Under the same precipitation scenario, the reaction rate only had a minor impact on the pre-exponential coefficient. The exponent (n) in the surface growth scenario, which was 0.41 ± 0.08 and 0.36 ± 0.09 for the two cases, was slightly larger than in the homogeneous nucleation scenario. For the three homogeneous nucleation cases, n showed a larger variation across different geometries, with values of 0.26 ± 0.09, 0.30 ± 0.13, and 0.29 ± 0.16. For FGeo8, simulations were performed with larger domain sizes for "ssa0.44_usgs" and "pga_usgs". The simulations showed similar evolution in the pore structures. The pre-exponential coefficient and exponent values were within the ranges observed for different geometries. More information is provided in the supporting information.

Diffusion simulations of the quartz pack geometries resulted in similar observations (Figure 5). The pre-exponential coefficient was lower than that of the Finney pack geometries. It was 0.22 ± 0.07, 0.3 ± 0.09, 0.26 ± 0.08 for "ssa0.44", "ssa0.44_usgs", and "ssa44", respectively, which was larger than the two surface growth

cases (0.11 ± 0.1 and 0.14 ± 0.1). The exponent values were 0.21 ± 0.2, 0.38 ± 0.22, 0.24 ± 0.15 for the three homogeneous nucleation cases, and were comparable to the average values of the Finney pack geometries. The exponent for the two surface growth cases were on the higher end of the range observed for the Finney pack geometries, with values of 0.47 ± 0.25 and 0.44 ± 0.21.

Everything else being equal, a smaller pre-exponential coefficient leads to a lower effective diffusivity. This is consistent with the observation that the pre-exponential coefficients of the quartz pack geometries, for which the initial diffusivity ranges between 3.2 and 7.2e−10 m^2/s, are systematically lower than those of the Finney pack geometries, for which the initial diffusivities are 1.1–1.6e−9 m^2/s. A weak positive correlation was observed between the pre-exponential coefficient and the initial diffusivity (supporting information). The exponent controls the shape of the curve described by Equation 11. A small exponent corresponds to a limited reduction in diffusivity at early stages of porosity reduction and a sharp decrease toward the critical porosity. For instance, in the homogeneous nucleation scenario (for which the exponent tends to be lower), the initial development of the precipitation bands did not necessarily translate to transport pathway clogging and thus reduction in the diffusivity. In contrast, in the surface growth scenario, precipitation resulted in grain dilation very early on, the pore throats and thus diffusivity decreased continuously from the beginning of the simulations, corresponding to higher exponents. The trajectory of the diffusivity evolution depends on not only the precipitation mechanism but also the pore structures. This is why large standard deviations in the exponent were observed among different geometries. However, no clear correlation was observed between the exponent and the initial porosity or diffusivity in our simulations. Additional pore structure characteristics need to be examined in the future.

4. Discussion

Our work advances our understanding and predictive capability of precipitation driven alteration of porous media in two ways. The modeling workflow presented enables the prediction of precipitation as a result of the chemical gradients developed from pore structure heterogeneity and various chemical interactions, in comparison with assumed uniform precipitation or other prescribed precipitation patterns. It therefore gives a more truthful representation of the pore-scale dynamics. In addition, while considerable variations were observed in the precipitation patterns among different geometries and precipitation kinetic setups, the macroscopic $\Phi - D_{\text{eff}}$ relationship was fairly consistent across all the simulations. This observation confirms the possibility of using this mathematical relationship for upscaling.

Our study is nevertheless based on 2D simulations (given the prohibitively high computational cost for hundreds of full 3D simulations) of pore structures with fairly large pore sizes, whereas real systems involve three dimensional processes and smaller pore sizes, especially ones in which diffusion is the dominant transport mechanism. Regardless of these differences, we expect the major observations of our study to hold in a more general sense. For instance, in the experimental study of (Rajyaguru et al., 2019), a chalk was used as a proxy material to examine diffusion-reaction dynamics in low-permeability systems. The sample used in the experiment had a porosity of 45%, comparable to the ones used in our study. Although the median pore throat size was ∼0.66 μm, one order of magnitude lower than the resolution of our model, a thin precipitation disk was observed due to homogeneous nucleation of barite, similar to the precipitation band predicted in our simulations. More importantly, the experimental study also observed that the same amount of precipitates resulted in a larger reduction of the diffusivity when homogeneous nucleation was dominant. This was in contrast to when heterogeneous nucleation on the substrate (similar to the surface growth scenario in our simulations) was dominant, consistent with our observation that homogeneous nucleation results in higher Φ_c and lower porosity reduction. The traditional Archie's law has been extensively evaluated experimentally and numerically, and the same formulation has been recovered for 2D and 3D domains. But the exponent of Archie's law was found to be lower in 2D, approximately equal to 1, than in 3D, approximately equal to 2, for various 3D natural media (Hunt, 2004). Following these observations, we expect that Equation 11 is broadly applicable, but the coefficients may be different in 3D due to the different number of degrees of freedom or different level of disorder, in addition to varying with the precipitation scenario and pore geometries as shown in our simulations. In this section, we discuss some of the assumptions and limitations, with the objective of increasing clarity of the applicability of our results and highlighting some future research needs.

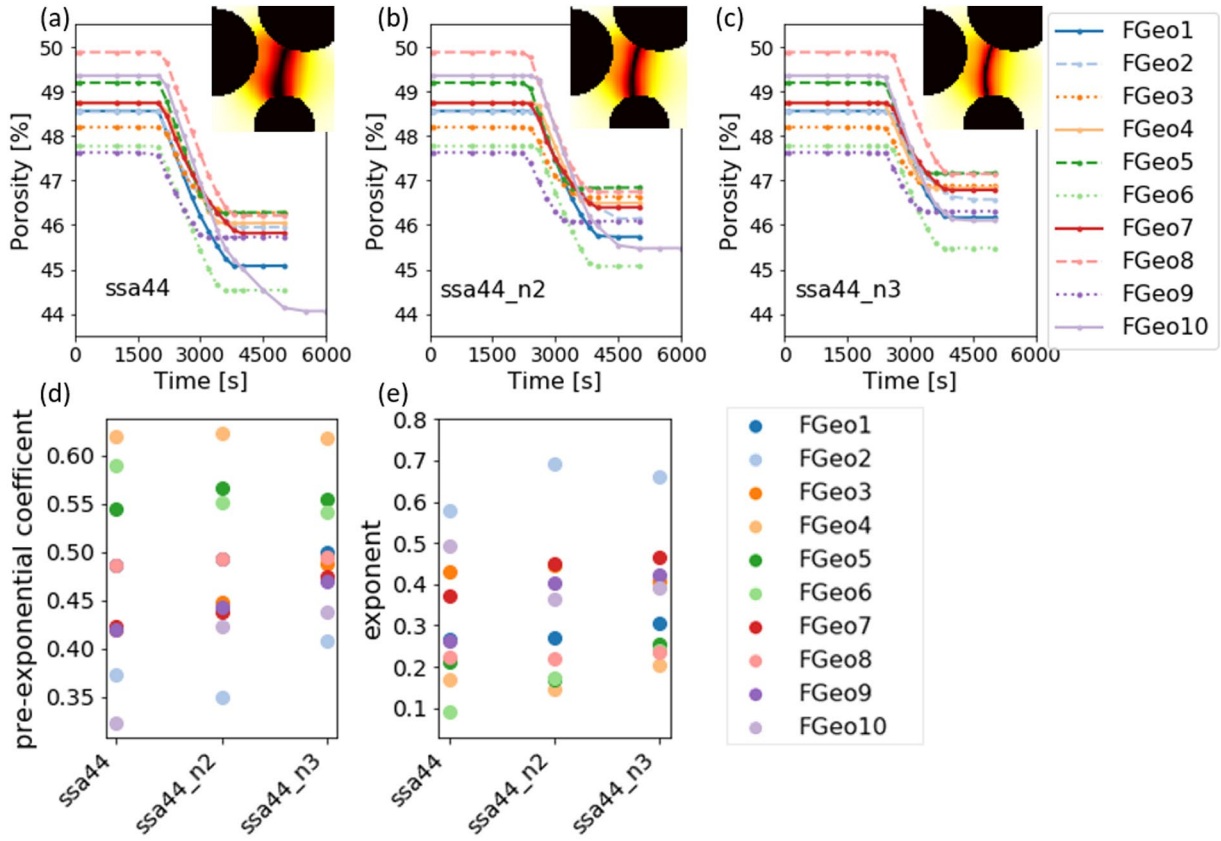

Figure 6. Comparison of the porosity evolution of 10 Finney pack geometries using the default linear grid-cell level tortuosity model (a), the nonlinear tortuosity model with exponent of 2 (b) and 3 (c), and the pre-exponential coefficient (d) and exponent (e) of the $\Phi - D_{\text{eff}}$ relationship of the three cases.

4.1. Impacts of Mineral Precipitation Mechanisms and Texture

Our simulations accounted for the impacts of pore geometry and precipitation kinetics of homogeneous nucleation and surface growth but did not resolve single crystals or the textures of the precipitates that can vary with nucleation and crystal growth mechanisms (Chen et al., 2014; Fazeli et al., 2020).

Additional simulations for 10 Finney pack geometries and the "ssa44" case were performed to evaluate how the texture of and thus tortuosity in the developing precipitates affect the macroscopic porosity-diffusivity evolution. These simulations used the non-linear relationships, $D_m\phi^2$ and $D_m\phi^3$, at the grid cell level, and showed the same trend as the linear tortuosity model simulations (Figure 6). However, for the higher exponents, the critical porosity (Φ_c) was larger, that is, the porosity reduction was smaller. Across the 10 geometries simulated, the reduction was 1.6%–3.9% and 1.3%–3.3% for the exponent of 2 and 3, respectively; compared to 1.9%–5.3% in the linear tortuosity model simulations. This is consistent with the conceptualization that a larger exponent results in increased loss of connectivity for a given amount of porosity reduction. Accordingly, the transport pathways are clogged at a faster speed even though the precipitation rate is the same, as illustrated by the thinner precipitation bands (Figures 6a–6c). The non-linear tortuosity model did not affect the pre-exponential coefficient of the $\Phi - D_{\text{eff}}$ relationship noticeably, which was 0.48 ± 0.08 and 0.50 ± 0.06 for the exponent of 2 and 3, respectively, or the exponent (n), which was 0.33 ± 0.17 and 0.36 ± 0.14 for the exponent of 2 and 3, respectively.

Another textural feature that may affect the macroscopic $\Phi - D_{\text{eff}}$ relationship is the "microporosity", that is, nanopores that remain in the precipitates due to reduced nucleation and precipitation rate under confinement. It has been reported that nucleation and precipitation in nanopores are prohibited or significantly reduced (Stack et al., 2014) because of the pore-size controlled solubility (PCS) effect (Emmanuel & Ague, 2009) or local transport limitations. If the PCS effect is dominant, and the diffusive

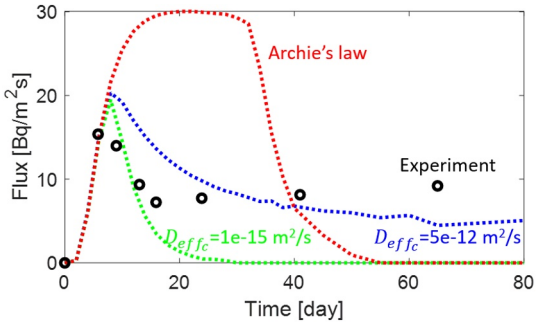

Figure 7. Tracer flux at the outlet. The experimental observations are shown in the open black circles, in comparison with simulation results using the traditional form of Archie's law (red dotted line) and using the revised relationship with D_{eff_c} = 1e−15 m^2/s (green dotted line) and D_{eff_c} = 5e−12 m^2/s (blue dotted line). The traditional Archie's law is given by $D_{\mathrm{eff}} = 1.3149\phi^2$, the exponent is the same as the revised relationship based on literature data, and the pre-exponential factor is determined based on the initial porosity and diffusivity reported in the experimental study.

transport through the nanopores is non-negligible, the mixing region and the precipitation bands will continue to grow until precipitation becomes undetectable, leading to phenomenological plugging of the system. The corresponding Φ_c is expected to be lower than what would be expected from our pore-scale simulations, whereas the corresponding D_{effc} will be constrained by the tortuosity in the precipitates and the thickness of the precipitation band, and is likely to be larger. In contrast, if the predominant mechanism for the remaining nanopores is local transport limitation, we may expect slight increase in Φ_c, and D_{effc} is by definition close to zero. However, in order to quantitatively evaluate the impacts of microporosity, information on the amount and tortuosity of the remaining nanopores is required. Thus, future studies on mechanistic understanding of various nucleation and crystal growth processes that contribute to the creation of microporosity and proper conceptualization of these processes in pore-scale models are needed.

4.2. Application of the Revised Relationship

The revised formulation (Equation 11) was implemented in 1D continuum simulations similar to Chagneau et al. (2015), for comparison with the column experiments. The 1D continuum model solves Equations 2, 4, 6, and 8 with equal discretization of 0.1 mm. Each grid cell is a combination of mineral grains and pore space with an initial porosity (Φ_{ini}) of 39% according to the CT image data. The precipitation rate follows the transition state theory rate law seeded with a tiny surface area initially. More details are documented in the supporting information. For the four parameters in Equation 11, the critical porosity (Φ_c) was set at 31% based on the post-reaction CT images. The exponent was set to be 2 according to prior studies of 3D natural rocks (Hunt, 2004; Navarre-Sitchler et al., 2009). The pre-exponential factor was constrained by the initial effective diffusivity (D_{effini}) of the column, that is, 4.48e−10 m^2/s:

$$a\left(\Phi_{\mathrm{ini}} - \Phi_c\right)^n = D_{\mathrm{effini}}. \tag{12}$$

There was no direct measurement of D_{effc}, and thus two values 1e−15 m^2/s and 5e−12 m^2/s were tested. The simulation results were compared with the effluent tracer flux and the amount of precipitates from the experiment.

In the experiment, tritiated water (HTO) was used as the tracer. The effluent flux peaked at ~15 Bq/m^{2}s around day 6 and stayed around 8 Bq/m^{2}s after day 15. The precipitates were observed in a ~6 mm zone and were largely located in a 0.35 mm thick disk, and amounted to 20–35 mg in different parallel experiments. Compared to the simple form of Archie's law, the revised relationship provides a better agreement with the experimental observations (Figure 7 and Table S1). The case of D_{eff_c} = 1e−15 m^2/s implicitly assumes that diffusion limitation is the only mechanism for precipitation termination as in the pore scale simulations. In this simulation, the precipitates were present in a ~7 mm zone and amounted to 20 mg by day 80. However, the flux went to zero after about 20 days. A D_{effc} of 5e−12 m^2/s effectively assumes the microporosity scenario due to PCS effect as discussed above. The presence of microporosity was implied by the variable gray values in the CT images collected in the experimental study (Chagneau et al., 2015), even though the individual pores constitute the microporosity were not resolved given the resolution of the images. In this case, the flux remained non-zero after the initial decrease and agreed well with the experimental observations. As the suppression of precipitation in microporosity was not explicitly modeled, the simulation adopts a simple treatment of setting the precipitation rate to zero when Φ_c was approached. The total amount of precipitates was ~113 mg within a ~9.5 mm zone. Both are larger than the low D_{effc} case given the higher diffusive flux and mixing. This over-estimation in precipitation may be attributed to sample heterogeneity along the column that was not considered, and that different precipitation mechanisms may be present in microporosity, that is, nano-pores.

5. Conclusions

In this study, we performed numerical investigation of pore-scale precipitation dynamics and their impacts on effective diffusivity (D_{eff}). The modeling results reproduced precipitation patterns that were observed in previous experiments. A precipitation band formed in the scenario of homogeneous nucleation, whereas the precipitates coated the grain surfaces in the surface growth scenario. For all geometries and precipitation rate setups simulated, the progress of the precipitation reaction led to the decrease of domain porosity (Φ) and D_{eff} until transport in the system was completely clogged. The surface growth scenario required more precipitation than the homogeneous nucleation scenario to clog the system and was largely influenced by the initial pore geometry. At a higher precipitation rate, the system was clogged with a smaller amount of the precipitate, that is, the critical porosity (Φ_c) was higher. Based on these observations, the $\Phi - D_{eff}$ relationship (traditional Archie's law) was revised to explicitly account for the clogging effect, that is, Φ_c and the critical effective diffusivity (D_{effc}) were included in the relationship. The two fitting parameters, the pre-exponential coefficient, and the exponent were between 0—1 for all simulations and showed large variations across different geometries. For the surface growth scenario, the exponent was slightly higher than for the homogeneous nucleation scenario. Application of this revised relationship in the 1D continuum scale model produced improved results that agree better with the column experiment compared to the traditional Archie's law. The amount of precipitation is still over-estimated, which indicates that other precipitation mechanisms may be present that reduced mineral precipitation. Future studies are needed to better understand processes such as precipitation under confinement and to conceptualize these processes for implementation in reactive transport models.

Data Availability Statement

All geometry data can be accessed through the digital rock portal (https://www.digitalrocksportal.org/). The fluid chemistry and thermodynamic and kinetic data are available in the cited references: Chagneau et al. (2015), Marty et al. (2015), Nielsen & Söhnel, (1971), Palandri (2004), and Poonoosamy et al. (2019). The code of CrunchTope is available at https://bitbucket.org/crunchflow/crunchtope-dev. Example input files and database for the CrunchTope simulation can be accessed at https://github.com/denghangPU/diffusion-dominated-pore-scale-precipitation.git.

Acknowledgments
The authors would like to acknowledge the funding support by the U.S. Department of Energy, Office of Fossil Energy, under Award Number DE-AC02-05CH11231, the Agence Nationale de la Recherche (ANR) under Contract No. ANR-18-CE05-0035-01, a grant overseen by the French National Research Agency (ANR) as part of the "Investissements d'Avenir" Program LabEx VOLTAIRE, 10-LABX-0100, and the European Union's Horizon 2020 research and innovation program under Grant Agreement No. 847593.

References

Cai, J., Wei, W., Hu, X., & Wood, D. A. (2017). Electrical conductivity models in saturated porous media: A review. *Earth-Science Reviews*, *171*, 419–433. https://doi.org/10.1016/j.earscirev.2017.06.013

Chagneau, A., Claret, F., Enzmann, F., Kersten, M., Heck, S., Made, B., & Schafer, T. (2015). Mineral precipitation-induced porosity reduction and its effect on transport parameters in diffusion-controlled porous media. *Geochemical Transactions*, *16*. https://doi.org/10.1186/s12932-015-0027-z

Chen, H. L., & Park, E. (2017). Reduction in contaminant mass flux with induced oxide mineral precipitation in quasi-multidimensional systems. *Environmental Earth Sciences*, *76*(14), 8. https://doi.org/10.1007/s12665-017-6807-2

Chen, L., Kang, Q., Carey, B., & Tao, W.-Q. (2014). Pore-scale study of diffusion-reaction processes involving dissolution and precipitation using the lattice Boltzmann method. *International Journal of Heat and Mass Transfer*, *75*, 483–496. https://doi.org/10.1016/j.ijheatmasstransfer.2014.03.074

Cil, M. B., Xie, M., Packman, A. I., & Buscarnera, G. (2017). Solute mixing regulates heterogeneity of mineral precipitation in porous media. *Geophysical Research Letters*, *44*(13), 6658–6666. https://doi.org/10.1002/2017gl073999

Deng, H., Molins, S., Trebotich, D., Steefel, C., & DePaolo, D. (2018). Pore-scale numerical investigation of the impacts of surface roughness: Upscaling of reaction rates in rough fractures. *Geochimica et Cosmochimica Acta*, *239*, 374–389. https://doi.org/10.1016/j.gca.2018.08.005

Emmanuel, S., & Ague, J. J. (2009). Modeling the impact of nano-pores on mineralization in sedimentary rocks. *Water Resources Research*, *45*, 12. https://doi.org/10.1029/2008wr007170

Emmanuel, S., & Berkowitz, B. (2005). Mixing-induced precipitation and porosity evolution in porous media. *Advances in Water Resources*, *28*(4), 337–344. https://doi.org/10.1016/j.advwatres.2004.11.010

Fazeli, H., Masoudi, M., Patel, R. A., Aagaard, P., & Hellevang, H. (2020). Pore-scale modeling of nucleation and growth in porous media. *ACS Earth and Space Chemistry*, *4*(2), 249–260. https://doi.org/10.1021/acsearthspacechem.9b00290

Finney, J. (2016). Finney packing of spheres. In Digital Rocks Portal. https://doi.org/10.5194/acp-2016-59-ac1

Garcia-Rios, M., Luquot, L., Soler, J. M., & Cama, J. (2015). Influence of the flow rate on dissolution and precipitation features during percolation of CO2-rich sulfate solutions through fractured limestone samples. *Chemical Geology*, *414*, 95–108. https://doi.org/10.1016/j.chemgeo.2015.09.005

Griffiths, L., Heap, M. J., Wang, F., Daval, D., Gilg, H. A., Baud, P., et al. (2016). Geothermal implications for fracture-filling hydrothermal precipitation. *Geothermics*, *64*, 235–245. https://doi.org/10.1016/j.geothermics.2016.06.006

Hunt, A. G. (2004). Continuum percolation theory and Archie's law. *Geophysical Research Letters*, *31*(19), 4. https://doi.org/10.1029/2004gl020817

Kim, D. H., Mahabadi, N., Jang, J., & van Paassen, L. A. (2020). Assessing the kinetics and pore-scale characteristics of biological calcium carbonate precipitation in porous media using a microfluidic chip experiment. *Water Resources Research*, *56*(2), 19. https://doi.org/10.1029/2019wr025420

Li, Q., Steefel, C. I., & Jun, Y.-S. (2017). Incorporating nanoscale effects into a continuum-scale reactive transport model for CO2-deteriorated cement. *Environmental Science & Technology*, *51*(18), 10861–10871. https://doi.org/10.1021/acs.est.7b00594

Lichtner, P. C. (1996). Chapter 1. Continuum formulation of multicomponent-multiphase reactive transport. In P. C. Lichtner, C. I. Steefel, & E. H. Oelkers (Eds.), *Reactive transport in porous media* (pp. 1–82). https://doi.org/10.1515/9781501509797-004

Luquot, L., & Gouze, P. (2009). Experimental determination of porosity and permeability changes induced by injection of CO2 into carbonate rocks. *Chemical Geology*, *265*(1–2), 148–159. https://doi.org/10.1016/j.chemgeo.2009.03.028

Marty, N. C. M., Claret, F., Lassin, A., Tremosa, J., Blanc, P., Madé, B., et al. (2015). A database of dissolution and precipitation rates for clay-rocks minerals. *Applied Geochemistry*, *55*, 108–118. https://doi.org/10.1016/j.apgeochem.2014.10.012

Matter, J. M., Stute, M., Snaebjornsdottir, S. O., Oelkers, E. H., Gislason, S. R., Aradottir, E. S., et al. (2016). Rapid carbon mineralization for permanent disposal of anthropogenic carbon dioxide emissions. *Science*, *352*(6291), 1312–1314. https://doi.org/10.1126/science.aad8132

Menke, H. P., Bijeljic, B., & Blunt, M. J. (2017). Dynamic reservoir-condition microtomography of reactive transport in complex carbonates: Effect of initial pore structure and initial brine pH. *Geochimica et Cosmochimica Acta*, *204*, 267–285. https://doi.org/10.1016/j.gca.2017.01.053

Molins, S., Soulaine, C., Prasianakis, N. I., Abbasi, A., Poncet, P., Ladd, A. J. C., et al. (2020). Simulation of mineral dissolution at the pore scale with evolving fluid-solid interfaces: Review of approaches and benchmark problem set. *Computational Geosciences*. https://doi.org/10.1007/s10596-019-09903-x

Molnar, I. L. (2016). Uniform quartz - Silver nanoparticle injection experiment. In *Digital rocks portal*. https://doi.org/10.1063/1.4965587

Nachshon, U., Shahraeeni, E., Or, D., Dragila, M., & Weisbrod, N. (2011). Infrared thermography of evaporative fluxes and dynamics of salt deposition on heterogeneous porous surfaces. *Water Resources Research*, *47*, W12519. https://doi.org/10.1029/2011WR010776

Navarre-Sitchler, A., Steefel, C. I., Yang, L., Tomutsa, L., & Brantley, S. L. (2009). Evolution of porosity and diffusivity associated with chemical weathering of a basalt clast. *Journal of Geophysical Research*, *114*. https://doi.org/10.1029/2008jf001060

Nielsen, A. E., & Söhnel, O. (1971). Interfacial tensions electrolyte crystal-aqueous solution, from nucleation data. *Journal of Crystal Growth*, *11*(3), 233–242. https://doi.org/10.1016/0022-0248(71)90090-x

Noiriel, C., Steefel, C. I., Yang, L., & Ajo-Franklin, J. (2012). Upscaling calcium carbonate precipitation rates from pore to continuum scale. *Chemical Geology*, *318–319*, 60–74. https://doi.org/10.1016/j.chemgeo.2012.05.014

Noiriel, C., Steefel, C. I., Yang, L., & Bernard, D. (2016). Effects of pore-scale precipitation on permeability and flow. *Advances in Water Resources*, *95*, 125–137. https://doi.org/10.1016/j.advwatres.2015.11.013

Otsu, N. (1979). A threshold selection method from gray-level histograms. *IEEE Transactions on Systems, Man, and Cybernetics*, *9*(1), 62–66. https://doi.org/10.1109/tsmc.1979.4310076

Palandri, J. L. (2004). A compilation of rate parameters of water-mineral interaction kinetics for application to geochemical modeling [electronic resource]/by James L. Palandri and Yousif K. Kharaka, *prepared in cooperation with the National Energy Technology Laboratory*. Menlo Park, Calif: United States Department of Energy, U.S. Departtment of the Interior, U.S. Geological Survey. https://doi.org/10.3133/ofr20041068

Peng, S., Hu, Q. H., & Hamamoto, S. (2012). Diffusivity of rocks: Gas diffusion measurements and correlation to porosity and pore size distribution. *Water Resources Research*, *48*, 9. https://doi.org/10.1029/2011wr011098

Poonoosamy, J., Westerwalbesloh, C., Deissmann, G., Mahrous, M., Curti, E., Churakov, S. V., et al. (2019). A microfluidic experiment and pore scale modelling diagnostics for assessing mineral precipitation and dissolution in confined spaces. *Chemical Geology*, 528.

Prasianakis, N. I., Curti, E., Kosakowski, G., Poonoosamy, J., & Churakov, S. V. (2017). Deciphering pore-level precipitation mechanisms. *Scientific Reports*, *7*. https://doi.org/10.1038/s41598-017-14142-0

Rahardianto, A., McCool, B. C., & Cohen, Y. (2008). Reverse osmosis desalting of inland brackish water of high gypsum scaling propensity: Kinetics and mitigation of membrane mineral scaling. *Environmental Science & Technology*, *42*(12), 4292–4297. https://doi.org/10.1021/es702463a

Rajyaguru, A., L'Hôpital, E., Savoye, S., Wittebroodt, C., Bildstein, O., Arnoux, P., et al. (2019). Experimental characterization of coupled diffusion reaction mechanisms in low permeability chalk. *Chemical Geology*, *503*, 29–39. https://doi.org/10.1016/j.chemgeo.2018.10.016

Seigneur, N., Mayer, K. U., & Steefel, C. I. (2019). Reactive transport in evolving porous media. *Reviews in Mineralogy and Geochemistry*, *85*, 197–238. https://doi.org/10.2138/rmg.2019.85.7

Singurindy, O., Berkowitz, B., & Lowell, R. P. (2004). Carbonate dissolution and precipitation in coastal environments: Laboratory analysis and theoretical consideration. *Water Resources Research*, *40*(4), 13. https://doi.org/10.1029/2003wr002651

Smith, M. M., Sholokhova, Y., Hao, Y., & Carroll, S. A. (2013). CO_2-induced dissolution of low permeability carbonates. Part I: Characterization and experiments. *Advances in Water Resources*, *62*, 370–387. https://doi.org/10.1016/j.advwatres.2013.09.008

Soulaine, C., Roman, S., Kovscek, A., & Tchelepi, H. A. (2017). Mineral dissolution and wormholing from a pore-scale perspective. *Journal of Fluid Mechanics*, *827*, 457–483. https://doi.org/10.1017/jfm.2017.499

Stack, A. G., Fernandez-Martinez, A., Allard, L. F., Bañuelos, J. L., Rother, G., Anovitz, L. M., et al. (2014). Pore-size-dependent calcium carbonate precipitation controlled by surface chemistry. *Environmental Science & Technology*, *48*(11), 6177–6183. https://doi.org/10.1021/es405574a

Steefel, C. I., Appelo, C. A. J., Arora, B., Jacques, D., Kalbacher, T., Kolditz, O., et al. (2015). Reactive transport codes for subsurface environmental simulation. *Computational Geosciences*, *19*(3), 445–478. https://doi.org/10.1007/s10596-014-9443-x

Steefel, C. I., Beckingham, L. E., & Landrot, G. (2015). Micro-continuum approaches for modeling pore-scale geochemical processes. *Reviews in Mineralogy and Geochemistry*, *80*, 217–246. https://doi.org/10.2138/rmg.2015.80.07

Steefel, C. I., DePaolo, D. J., & Lichtner, P. C. (2005). Reactive transport modeling: An essential tool and a new research approach for the Earth sciences. *Earth and Planetary Science Letters*, *240*(3–4), 539–558. https://doi.org/10.1016/j.epsl.2005.09.017

Steefel, C. I., & Lasaga, A. C. (1994). A coupled model for transport of multiple chemical species and kinetic precipitation/dissolution reactions with application to reactive flow in single phase hydrothermal systems. *American Journal of Science*, *294*(5), 529–592. https://doi.org/10.2475/ajs.294.5.529

Steefel, C. I., & Lichtner, P. C. (1994). Diffusion and reaction in rock matrix bordering a hyperalkaline fluid-filled fracture. *Geochimica et Cosmochimica Acta*, *58*(17), 3595–3612. https://doi.org/10.1016/0016-7037(94)90152-x

Steefel, C. I., & Lichtner, P. C. (1998). Multicomponent reactive transport in discrete fractures: I. Controls on reaction front geometry. *Journal of Hydrology*, *209*(1–4), 186–199. https://doi.org/10.1016/s0022-1694(98)00146-2

Steinwinder, J., & Beckingham, L. E. (2019). Role of pore and pore-throat distributions in controlling permeability in heterogeneous mineral dissolution and precipitation scenarios.*Water Resources Research*, *55*(7), 5502–5517. https://doi.org/10.1029/2019wr024793

Tartakovsky, A. M., Redden, G., Lichtner, P. C., Scheibe, T. D., & Meakin, P. (2008). Mixing-induced precipitation: Experimental study and multiscale numerical analysis. *Water Resources Research*, *44*(6). https://doi.org/10.1029/2006wr005725

Vankeuren, A. N. P., Hakala, J. A., Jarvis, K., & Moore, J. E. (2017). Mineral reactions in shale gas reservoirs: Barite scale formation from reusing produced water as hydraulic fracturing fluid. *Environmental Science & Technology*, *51*(16), 9391–9402.

Wright, R. N., Hartmann, T., & Fujita, Y. (2011). Inducing mineral precipitation in groundwater by addition of phosphate. *Geochemical Transactions*, *12*, 8. https://geochemicaltransactions.biomedcentral.com/articles/10.1186/1467-4866-12-8

Xie, M., Mayer, K. U., Claret, F., Alt-Epping, P., Jacques, D., Steefel, C., et al. (2015). Implementation and evaluation of permeability-porosity and tortuosity-porosity relationships linked to mineral dissolution-precipitation. *Computers & Geosciences*, *19*(3), 655–671. https://doi.org/10.1007/s10596-014-9458-3

Yoon, H., Valocchi, A. J., Werth, C. J., & Dewers, T. (2012). Pore-scale simulation of mixing-induced calcium carbonate precipitation and dissolution in a microfluidic pore network. *Water Resources Research*, *48*(2). https://doi.org/10.1029/2011wr011192

Zhang, C., Dehoff, K., Hess, N., Oostrom, M., Wietsma, T. W., Valocchi, A. J., et al. (2010). Pore-scale study of transverse mixing induced CaCO3 precipitation and permeability reduction in a model subsurface sedimentary system. *Environmental Science & Technology*, *44*(20), 7833–7838. https://doi.org/10.1021/es1019788

Zhang, C., Kang, Q., Wang, X., Zilles, J. L., Müller, R. H., & Werth, C. J. (2010). Effects of pore-scale heterogeneity and transverse mixing on bacterial growth in porous media. *Environmental Science & Technology*, *44*(8), 3085–3092. https://doi.org/10.1021/es903396h

Zou, C., Zhu, R., Liu, K., Su, L., Bai, B., Zhang, X., et al. (2012). Tight gas sandstone reservoirs in China: Characteristics and recognition criteria. *Journal of Petroleum Science and Engineering*, *88–89*, 82–91. https://doi.org/10.1016/j.petrol.2012.02.001